DNA Origami Characterized via Solid-State Nanopore: Insights into Nanostructure Dimensions, Rigidity and Yield

Liqun He,[‡1] Martin Charron,[‡1] Philipp Karau,[1] Kyle Briggs,[1] Jonathan Adams,[2] Hendrick de Haan,[2] Vincent Tabard-Cossa[*1]

‡ These authors contributed equally

[*]Corresponding author: tcossa@uottawa.ca

[1]Department of Physics, University of Ottawa, Ottawa, Ontario, Canada

[2]Faculty of Science, Ontario Tech University, Oshawa, Ontario, Canada

Abstract

Due to their programmability via specific base pairing, self-assembled DNA origami structures have proven to be useful for a wide variety of applications, including diagnostics, molecular computation, drug delivery, and therapeutics. Measuring and characterizing these structures is therefore of great interest and an important part of quality control. Here, we show the extent to which DNA nanostructures can be characterized by a solid-state nanopore; a non-destructive, label-free, single-molecule sensor capable of electrically detecting and characterizing charged biomolecules. We demonstrate that in addition to geometrical dimensions, nanopore sensing can provide information on the mechanical properties, assembly yield, and stability of DNA nanostructures. For this work, we use a model structure consisting of a 3 helix-bundle (3HB), *i.e.* three interconnected DNA double helices using a M13 scaffold folded twice on itself by short DNA staple strands, and translocate it through solid-state nanopores fabricated by controlled breakdown. We present detailed analysis of the passage characteristics of 3HB structures through nanopores under different experimental conditions which suggest that segments of locally higher flexibility are present along the nanostructure contour that allow for

the otherwise rigid 3HB to fold inside nanopores. By characterizing partially melted 3HB structures, we find that locally flexible segments are likely due to short staple oligomers missing from the fully assembled structure. The 3HB used herein is a prototypical example to establish nanopores as a sensitive, non-destructive, and label-free alternative to conventional techniques such as gel electrophoresis with which to characterize DNA nanostructures.

Introduction

Significant advances have been made in the field of DNA nanotechnology since its introduction.[1–6] The fabrication of nanoscale objects using DNA oligomers as building blocks is attracting a growing number of scientists from different disciplines looking to create a variety of 2-dimensional (2D) and 3-dimensional (3D) DNA nanostructures for diagnostics, therapeutics, and single-molecule biophysics applications.[7–14] While the programmable self-assembly process of DNA is highly efficient, it is also a highly complex thermodynamic process and the end product must usually be characterized to ascertain yield and structural consistency with the desired DNA nanostructure.[15]

DNA origami structures are characterized using a variety of techniques such as gel electrophoresis, transmission electron microscopy (TEM), atomic force microscopy (AFM), or Förster resonance energy transfer (FRET) microscopy.[15] Gel electrophoresis has been the gold standard for the characterization of DNA nanostructures given its simplicity and low cost. It provides rapid bulk estimation on the yield and purity of the assembly process but does not provide information about the correct assembly of the entire structure. Despite these shortcomings, gel electrophoresis remains a staple technique due to its non-destructive nature and is a popular tool for purification of assembled structures. Microscopy techniques, on the other hand, provide high resolution imaging of the sample at the single-molecule level and give information about the correctness of the assembly of 2D and 3D nanostructures. However, the sample preparation and experimental procedures of these techniques are invasive and can disrupt the structural integrity of the assembled products.[2,16–22]

Over the last few years, several studies have involved the characterization of DNA nanostructures using solid-state nanopores,[23–25] primarily for the development of biosensing,[26–33] and next-generation molecular data storage applications.[34–36] In a typical nanopore experiment, a membrane containing a nanometer-sized pore is placed between two electrolyte-filled compartments. When a voltage is applied across the membrane, ionic current flows through the nanopore. As individual nanostructures translocate through the pore, a modulation in ionic currents is observed. The extracted blockage depth, duration, frequency, and temporal structure of translocation events reveals structural information (size, conformation, shape) about the molecular structures of interest and their abundance. The nanopore approach has distinct advantages as a characterization tool for DNA nanostructures: It allows for the detection from bulk solution which preserves the structural features of the sample as opposed to immobilizing it on a surface and drying it; detection is performed label-free without the use of optical dyes, which can affect mechanical properties and functions;[37,38] given their single-molecule sensitivity, nanopores consume low amount of materials, with most current fluidic cells requiring low volumes (~1-10 µL) and as little as 1 ng or on the order of femtomoles of sample to operate in the high pM to low nM range for a single nanopore to collect a 100-1000 events in minutes.

Here, we demonstrate how solid-state nanopore sensing can be used as an analytical platform to characterize DNA nanostructure properties beyond geometry and yield. As a prototypical example, we characterize the electrophoretic capture and translocation characteristics of a 3 helix-bundle (3HB) nanostructure in various experimental conditions (salt, voltage, and pore size), and show through identification and characterization of nanopore translocation events that we are able to extract information about geometry, local mechanical properties, and assembly yield. Notably, we demonstrate that statistics of folded translocations can yield information regarding the local rigidity of molecules folding inside nanopores. Our results and interpretation of the folding kinetics of 3HB nanostructures in pores suggest that structures folding through pores have a non-uniform rigidity. By degrading 3HB samples using heat, we further show that such heterogeneous rigidity can arise from defects such as missing staple oligomers. The data presented here therefore demonstrate the extent by which solid-state nanopores can be used to characterize DNA nanostructures, shed light on the kinetics of folded

nanopore transport, and show how local missing oligomers arising from thermodynamic effects can affect structural properties of DNA nanostructures that may otherwise pass other quality-control metrics.

Results and Discussion

3HB assembly and Nanopore Characterization

In this work, we used a three-helix DNA bundle (3HB) as our model DNA nanostructure, which consists of three parallel dsDNA double-helices bound together. More precisely, 190 short single-stranded DNA (ssDNA) oligomers hybridize to different locations of a 7249 nucleotide-long linearized single-stranded m13mp18 DNA, resulting in the scaffold folding twice on itself, as sketched in Figure 1a. The resulting structure is therefore expected to have a contour length of ~820 nm, a cross-sectional area at any point along its contour corresponding to three times that of double-stranded DNA (dsDNA), and have side-to-side distance of ~6 nm, due to the hexagonal pattern used to build the structure (Figure 1b).[39] The protocols employed, the design and the sequences of the structures are described in the Methods Section and in Supplementary Sections S1 and S2, respectively. Once assembled, the structures were characterized by gel electrophoresis, through which assembly quality was verified by confirming the presence of only one band, as shown in Figure 1c.

For all experiments shown here, 3HB structures were electrophoretically driven through nanopores (Figure 1d) fabricated by the controlled breakdown method.[40,41] Experiments were performed with pores (n = 11) of different sizes (9 – 15 nm), in different salt concentrations (0.45 – 3.6 M LiCl), and under a wide range of voltages (100 - 900 mV). As an example, Figure 1e shows concatenated current traces of current blockages induced by 3HB structures in a 13.2 nm pore, under a 200 mV bias in 1.2 M LiCl salt. The current trace from each detected blockade event is then fitted (See Methods) to extract metrics useful for characterization, such as maximum conductance blockage depth reached during a blockade event ΔG_{max}, and the total translocation time τ, as shown in Figure 1e. A typical example of nanopore data visualization is displayed in Figure 1f, which shows a scatterplot of ΔG_{max} *versus* τ, for 486 single molecule events. As will be discussed in the following sections, the information contained in such data is diverse and can

be related to the nanostructure geometry, structure, or to the different ways a molecule can enter a pore.

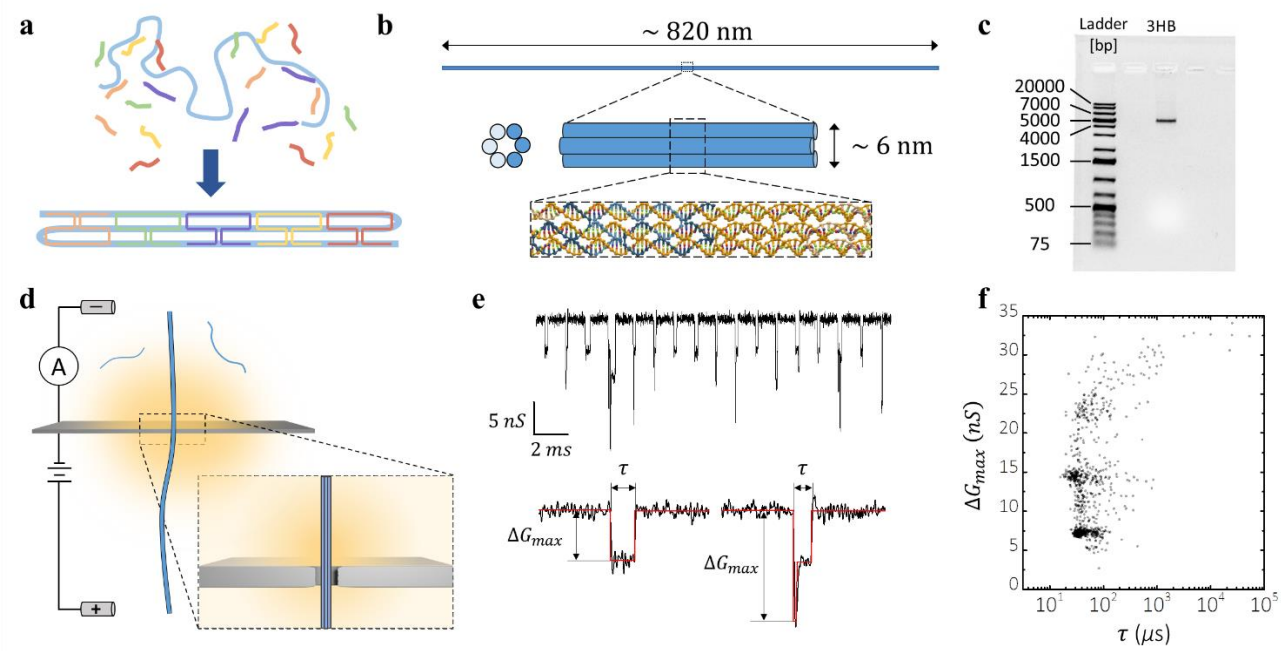

Figure 1. DNA nanostructure assembly and characterization with nanopore. a) Schematic of DNA helix bundle hybridization: thermal annealing of 7249 nt M13mp13 with 190 short "staple" strands. b) Expected dimensions, and structure of 3-Helix bundle assembly. c) 1% agarose gel electrophoresis showing a ladder of various DNA lengths in one lane and fully assembled 3HB structures in the other. d) Setup for nanopore sensing of 3HB structures. Yellow hue depicts the electric field strength. e) Concatenated current traces of transient ionic blockades induced by the presence of 3HB in 1.2M LiCl under 200 mV in a 13.2nm pore (top). Individual blockade events fit to extract variables such as maximum conductance blockage, and translocation time (bottom). f) Scatterplot of maximum conductance blockage *versus* translocation time in the same experimental conditions as in (e), N = 846.

3HB Dimensions

To better interpret Figure 1f, Figure 2a replots the same data, *i.e.* 3HB in 1.2 M LiCl in a 13.2 nm pore under a 200 mV bias, with blockages normalized by ΔG_{DNA}, the blockage level of single-file dsDNA. Here, $\Delta G_{DNA} = 1.54\,nS$, and is obtained from the average maximum conductance blockage value measured from the translocations of 2 kbp dsDNA fragments inside the same pore. Figure 2a also plots a histogram of $\Delta G_{max}/\Delta G_{DNA}$, from which three peaks can easily be identifiable. Fitting those three peaks to normal distributions we find each peak to have mean and standard deviation values of:

$$\Delta G_1 \pm \sigma_1 = (3.1 \pm 0.2) \times \Delta G_{DNA}$$
$$\Delta G_2 \pm \sigma_2 = (6.2 \pm 0.4) \times \Delta G_{DNA}$$
$$\Delta G_3 \pm \sigma_3 = (9.9 \pm 0.6) \times \Delta G_{DNA}$$

The shallowest population has a mean blockage ΔG_1 equal to $3.1 \times \Delta G_{DNA}$, which corresponds precisely to the blockage expected from single-file translocation of properly assembled 3HB structures, whose cross-sectional area should be three times that of dsDNA, and therefore block current three times as much when inside the pore. Interestingly, the two other populations appear to be quantized and show $\Delta G_2 \approx 2 \times \Delta G_1$, and $\Delta G_3 \approx 3 \times \Delta G_1$. Such quantized blockages are commonly observed for dsDNA translocations[42] and correspond to folded passages, *i.e.* translocations for which multiple segments of an individual molecule are inside the pore at once. These folded translocations can occur for example if a polymer enters a pore not by one of its ends, but by bending somewhere along its contour. For 3HB experiments, quantized blockages were observed in all pores and under most voltages tested, as observed in Figure 2b, which shows $\Delta G_{max}/\Delta G_{DNA}$ histograms for a 9.3 nm pore in 0.9 M LiCl as a function of voltage.

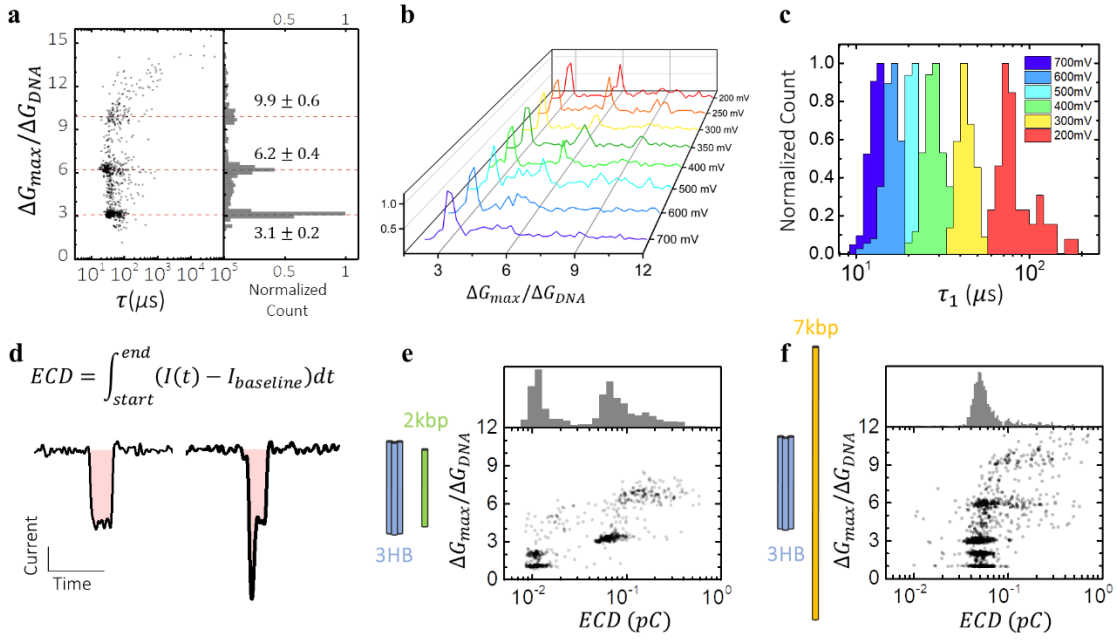

Figure 2. a) Scatter plot of maximum conductance blockage *versus* translocation time for 3HB in 1.2 M LiCl at 200 mV in a 13.2 nm pore (left). The maximum conductance blockage of 3HB blockades is normalized by ΔG_{DNA}, *i.e.* the maximum conductance blockage for 2 kbp dsDNA measured in the same nanopore. Distribution of normalized blockages (right). b) Distributions of maximum 3HB blockages measured under different voltages on a 9.3 nm pore

in 0.9 M LiCl. c) Translocation time distributions measured under different voltages for the same pore as in b). Only the durations of single-file translocations, $2 < \Delta G_{max}/\Delta G_{DNA} < 4$, are considered for statistics. d) Definition and visual representation of Equivalent Charge Deficit (ECD), *i.e.* the area in pink. e) ECD comparison of 3HB and 2 kbp dsDNA (similar length) in a 13.3 nm pore in 0.9 M LiCl under a 200 mV bias. f) ECD comparison of 3HB and 7 kbp dsDNA (similar # of bp) in an 11.2 nm pore in 0.9 M LiCl under a 200 mV bias.

To clarify the nature of the various blockades, we analyzed each ΔG_{max} sub-population, starting with the events from the ΔG_1 subpopulation. Figure 2c plots the normalized distributions of blockade durations τ_1 observed under different voltages for events from Figure 2b with blockages corresponding to $2 < \Delta G_{max}/\Delta G_{DNA} < 4$. Figure 2c shows a monotonic reduction of τ_1 with voltage. This is expected from full translocations from one side of the pore to the other as opposed to collisions, where molecules interact with the pore but remain on the same side of the membrane. Indeed, the blockage duration of molecules entering and fully traversing nanopores reduces under higher voltages due to increasing drift velocities, whereas the blockage duration arising from collisions with a pore increases with voltage due to the increased pulling force making it harder for molecules to diffuse away.[23,43] A voltage sweep obtained under a different salt concentration and pore size is shown in Supplementary Figure S3, and shows a similar monotonic voltage trend. Additionally, we characterized ΔG_1 events by measuring the dependence of translocation time on salt concentration and determined that similarly to dsDNA translocations,[44] 3HB structures translocate faster in lower salt concentrations (see Figure S4 of Supplementary Information).[45]

We further analyzed 3HB translocations by calculating their equivalent charge deficit (ECD), calculated as the time-integral of the difference between the current during the blockade event and the open-pore current (Figure 2d), which corresponds to the amount of charge that would have traversed the nanopore had the translocating molecule not blocked it.[30] For large nanopores with minimal molecular interactions with the pore wall, ECD values of folded and single-file translocations are nearly identical. ECD is therefore primarily related the volume of the translocating molecular structure, in addition to its mobility. Figures 2e-f show scatter plots of the maximum blockage $\Delta G_{max}/\Delta G_{DNA}$ *versus* ECD for a mixture of 3HB and 2 kbp dsDNA, two molecules of similar contour lengths ($L_{3HB} = 820\ nm$, $L_{2kbp} = 680\ nm$), and a mixture of 3HB

and 7 kbp dsDNA, two molecules of similar number of base pairs and thus volumes. These two experiments were done in nanopores of 13.3 nm (Figure 2e) and 11.2 nm (Figure 2f), in 0.9 M LiCl under a bias of 200 mV. The normalized ECD distribution of each mixture is shown above the corresponding scatterplot in Figures 2e-f. The ECD distribution of 2 kbp dsDNA is significantly smaller than 3HB, whereas the ECD distributions of 7 kbp dsDNA and 3HB overlap. This is expected since 3HB structures are assembled by hybridizing staple strands to a 7249 nt ssDNA scaffold, resulting in a volume similar to that of a 7 kbp dsDNA. Figure S5 in the Supplementary Information further demonstrates the sensitivity of such comparisons by showing that the ECD distributions of 3HB and 10 kbp dsDNA are separable.

From the combined observations obtained from Figure 2, we conclude that blockade events from ΔG_1, *i.e.* the sub-population centered around $\Delta G_{max}/\Delta G_{DNA} \approx 3$, result from translocations of molecules with cross-sectional areas three times that of dsDNA, and volumes similar to 7 kbp dsDNA. These dimensions correspond exactly to those expected from properly assembled 3HB structures passing through nanopores in a single-file manner. Note that ECD values from ΔG_2 and ΔG_3 3HB populations in Figures 2e-f are slightly larger than those of ΔG_1 or 7 kbp dsDNA. This either points to increased pore-polymer interactions, or at more complex dynamics.

3HB Folding – Metastable State

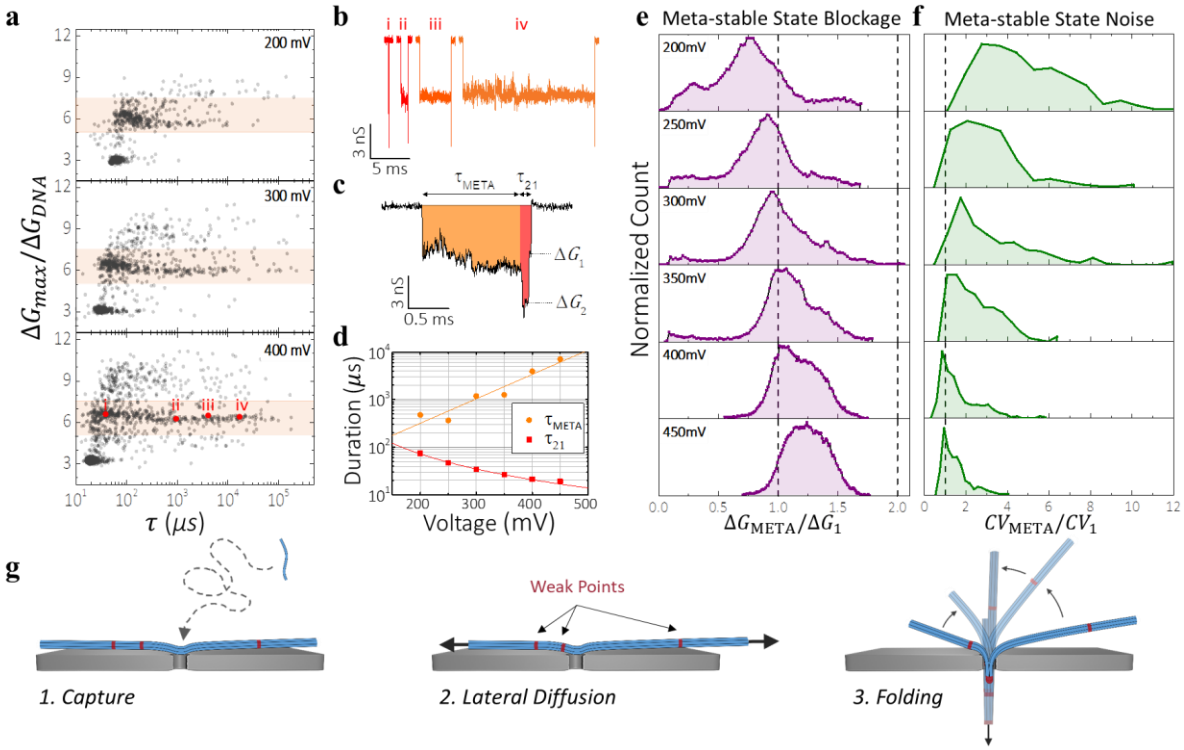

Figure 3. Folding statistics of 3HB translocations in a 13.3 nm pore in 0.9 M LiCl. a) Scatter plots of maximum blockage level *versus* translocation time measured at 200 mV, 300 mV, and 400 mV. Red dots and roman numerals identify which events are shown in b). b) Current traces of four events with $\Delta G_{max} = 2\Delta G_{3HB} \approx 6\Delta G_{DNA}$ of various durations. Events are from the 400 mV data set shown in a). c) Representative current trace of a folded 3HB translocation event preceded by a meta-stable state. Orange portion represents the meta-stable state, which is followed by a folded state and single-file state shown in red. d) Duration of meta-stable (orange dots) and folded translocation states (red squares) as a function of applied voltage. e) Histograms of meta-stable state blockage level, normalized by single-file 3HB translocation blockage ΔG_{3HB} for 200, 250, 300, 350, 400, and 450 mV. The histograms were obtained by averaging the area-normalized conductance histograms of each individual event. f) Histograms of the coefficient of variation (CV) of the nanopore conductance during the metastable states, CV_{META}. Values are normalized by the CV measured during single-file 3HB translocations, CV_{3HB}. Measurements under 200, 250, 300, 350, 400, and 450 mV are shown. g) Illustrations of the proposed translocation process of folded 3HB.

After establishing that events from the ΔG_1 population result from single-file translocations of properly assembled 3HB nanostructures, we next investigated the blockade events from the ΔG_2 sub-population: events with maximum blockages corresponding to six times that of dsDNA, *i.e.* $\Delta G_{max} \approx 6 \times \Delta G_{DNA}$, or equivalently to twice that of single-file 3HB translocations. Figure 3a plots the normalized maximum blockage level $\Delta G_{max}/\Delta G_{DNA}$ of individual 3HB translocations *versus* the corresponding translocation times for a 13.3 nm pore in

0.9 M LiCl under 200, 300 and 400 mV. Consistent with Figure 2a, different populations can be identified based on maximum level blockage alone. The ΔG_2 sub-population ($5 < \Delta G_{max}/\Delta G_{DNA} < 7.5$) is highlighted in Figure 3a to better visualize its response to different voltages.

The three different voltages displayed in Figure 3a show that events in the ΔG_2 population behave differently than single-file translocations: Whereas the blockage duration of some translocations gets shorter with increasing voltage, as expected from full translocations (Figure 2c), the blockage duration of other events increases with voltage, as expected from collision-like events. Under a bias of 400 mV, some events have translocation times up to 2-3 orders of magnitude longer than 200 mV events. These two confounding behaviors result in a spread of τ that significantly increases with voltage, as seen in Figure 3a. This behavior was observed in other high-voltage nanopore experiments and is not unique to this single-data set.

Insight into the nature of this sub-population of 3HB with $\Delta G_2 \approx 6 \times \Delta G_{DNA}$ blockage level is gained by examining the current signature of individual blockade events. Figure 3b displays the traces of four events which span the entire range of translocation times (selected events are highlighted in red in Figure 3a). Interestingly, these events begin with a shallow blockage state, followed by a deeper one. In fact, more than $90\ \%$ of events from the ΔG_2 sub-population can be divided into three consecutive blockage states, as depicted in Figure 3c: an initial metastable state with a blockage depth (ΔG_{META}) which can be noisy and very long (up to $10^5\ \mu s$), followed by an intermediate blockage of depth ΔG_2 and a final blockage state of depth ΔG_1. These latter two states are expected of a folded translocation in which a 3HB molecule entered a pore not by an end, but by bending a segment along its contour inside the pore.[42,46] We therefore attribute these events in the ΔG_2 sub-population as folded 3HB translocations preceded by a metastable state. Indeed, Figure 3d plots the voltage dependence of metastable state durations τ_{META} and of the final two states $\tau_{21} = \tau - \tau_{META}$ (as also defined in Figure 3c), showing that τ_{21} monotonically reduces with voltages, and is well described by a power scaling law of the form $\tau_{21} \sim \Delta V^{(-1.8 \pm 0.1)}$, whereas τ_{META} monotonically increases with voltage, and is well described by an exponential function $\tau_{META} \sim e^{\Delta V/(85 \pm 10)mV}$. Just as for single-file translocations, the fact that τ_{21} reduces with voltage supports the interpretation that the two final blockage states correspond to a 3HB traversing the nanopore in a folded conformation.

Conversely, because of its increasing duration with increasing voltage, the metastable state is collision-like, and is hypothesized to result from the 3HB nanostructure lying across the pore opening. At high voltages, the metastable state dominates the event duration and is therefore responsible for the wide spread of translocation times observed in Figure 3a (see Figure S5 of Supplementary Information).

To better understand the nature and origin of the metastable state, we further investigated the properties of the current blockage observed during the metastable state. Figure 3e displays histograms of the metastable state conductance blockage ΔG_{META} measured under different voltages, normalized by ΔG_1 to reduce inter-measurement variability. Figure 3e shows that ΔG_{META} gets deeper for larger voltages, as shown by its most probable value increasing monotonically with voltage: At 200 mV, the most probable metastable state blockage value is $\Delta G_{META}/\Delta G_1 \approx 0.77$, whereas it is ≈ 1.21 at 450 mV. At lower voltages therefore, a 3HB nanostructure presumably lying above the pore blocks less current than if it were fully inserted into the nanopore (as for single-file translocations), whereas the opposite is true for higher voltages.

Figure 3f shows the histogram of the metastable state blockage noise measured at different voltages. Here the noise is quantified using the coefficient of variation $CV_{META} = \sigma_{META}/\mu_{META}$, *i.e.* the ratio of the metastable state standard deviation $\sigma_{META}^2 = \langle(\Delta G_{META} - \mu_{META})^2\rangle$ and mean $\mu_{META} = \langle\Delta G_{META}\rangle$ values. CV_{META} values are normalized by the average noise of single-file translocations CV_1, calculated in the same way. The relative metastable state noise is observed to reduce with increasing voltage. Interestingly, for higher voltages the noise reduces to the same values as for single-file 3HB translocations. In Supplementary Figure S8, it is further shown that the current blockage during the metastable state displays voltage-independent 1/*f* noise.

The voltage trends identified in Figure 3 help form a complete picture of the mechanism by which 3HB nanostructures fold inside nanopores: The bending and folding of 3HB inside nanopores is identified by the last two blockage states (Figure 3c), and is preceded by a collision-like metastable state which lasts longer (Figure 3d), blocks more current (Figure 3e), and gets less

noisy (Figure 3f) with increasing voltage. Based on these observations, we unravel the folding steps of 3HB as follows: 1) When a 3HB does not approach the nanopore by an end, it gets pulled down across the pore opening by the electric field at some intermediate position along its contour; 2) Due to its high local rigidity (persistence length $\ell_{3HB} > \ell_{DNA} > d_{pore}$), it does not bend inside the pore; It instead diffuses laterally, the action of which is hindered by the electric field in the vicinity of the pore, which acts to pin nanostructures against the pore mouth and membrane; 3) Through lateral diffusion, a segment of weaker local rigidity along the 3HB eventually finds the nanopore, which facilitates bending and entry inside the nanopore. A folded translocation subsequently occurs, wherein two 3HB segments are in the pore at once (folded state ΔG_2), followed by a single segment (unfolded state ΔG_1). See Figure 3g for a depiction of the proposed folding mechanism.

Similar docking phenomena have been previously described for dsDNA[47], observed for DNA nanostructures and for stiff filamentous viruses.[32,43,48–50] In this work, docking and diffusion prior to translocation helps explain the observations of Figures 3e and 3f: increasing voltage enhances the electrophoretic pull in the pore vicinity, and pins 3HB nanostructures more strongly to the pore mouth, which increases blockage, and reduces the amplitude of the thermal motion that contributes to the additional noise in the metastable state. Supplementary Information Section 8 provides addition discussion and experimental results under different experimental conditions to support this interpretation.

Proposing 3HB molecules with a spatially varying rigidity helps explaining the observation from Figure 3d in which τ_{META} increases with voltage. Consider a heterogeneous linear polymer with segments too rigid to instantly bend inside nanopores, separated by a random distribution of more flexible segments which, when in contact with the nanopore, rapidly bend and enter. Unlike a uniformly rigid structure, the time required for the molecule of non-uniform rigidity to bend inside a nanopore is not determined by the characteristic time it takes for the molecule to overcome the bending energy barrier, but is instead determined by how long it takes for a flexible segment to find the pore through lateral diffusion. At higher voltages, 3HB molecules should be pinned closer to the pore (Figure 3e), and the increased membrane-polymer interactions (friction)

should hinder lateral diffusion, therefore resulting in longer times required for flexible segments to find the pore.

Lateral diffusion prior to translocation is further supported by a number of events displaying the metastable state followed only by a single-file blockage state instead of a folded-translocation sequence. Such events were presumably docked onto the pore near their ends, diffused laterally until their ends entered the pore, resulting therefore in a single-file translocation, as characterized, and displayed in section S8 of the Supplementary Information. Furthermore, although the metastable state was observed in almost all experimental conditions tested, it was notably more prominent under high voltages and in low salt concentrations (See Figures S11 and S12 of the Supplementary Information), two conditions that increase the electrophoretic pull on the 3HB molecules and therefore pin it more against the pore.

Complex Folding of Degraded Nanostructures

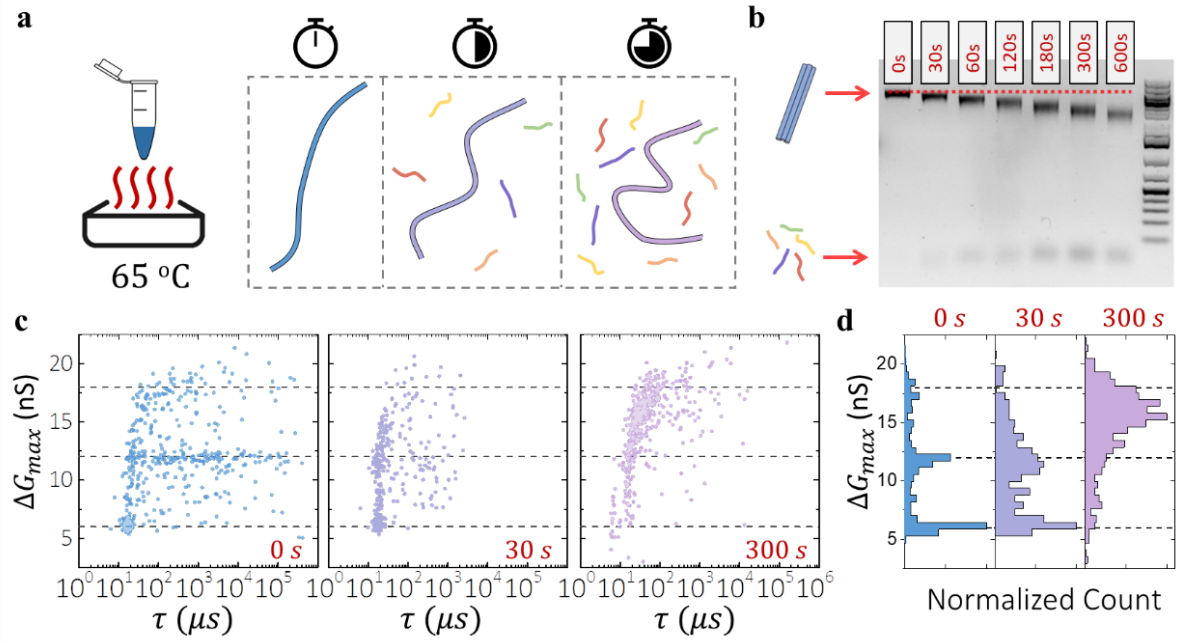

Figure 4. Nanopore characterization of heat-shocked 3HB. a) Sketch of 3HB structures heated at 65°C, gradually loosing staples. b) Gel electrophoresis of 3HB nanostructures thermally degraded for $0, 30, 60, 120, 180, 300,$ and 600 seconds and snap cooled to 4°C. 1 % Agarose gel in 1xTAE buffer (40 mM Tris, 20 mM acetic acid, and 2 mM EDTA) with an applied voltage of 70 V. Right lane: Generuler 1 kb plus DNA Ladder (ThermoFisher Scientific, SM1331). c) Scatter plots of Maximum conductance blockage level *versus* translocation time of 3HB structures heated at 65°C

for 0, 30, and 300 seconds for a 11.4 nm nanopore in 0.9 M LiCl with an applied bias of 400 mV. Single-file 3HB events produce a blockage level of $\sim 6\ nS$. Dash line are integers of the single-file level. d) Distributions of maximum conductance blockages from c).

The previous section proposed that the 3HB molecules have a heterogeneous rigidity, *i.e.* flexible segments scattered along the more rigid contour 3HB, to explain the mechanism by which 3HB folds inside nanopores. The experimental data of Figures 2 and 3 however offer no insight into the origin nor into the characteristics of such flexible segments. One possibility is that added flexibility arises from missing oligomer staples at different location along the length of the nanostructure. Unfortunately, individual missing oligomers cannot be mapped from the nanopore ionic current signal at this time due to the relatively fast translocations.

Here, to study the effect of missing oligomer staples on 3HB translocations, and the resulting of a non-homogeneously rigidity along 3HB contour, we purposefully induced partial melting of the staples by briefly heating the 3HB structures. Using a thermal cycler, samples of the same 3HB assembly batch were heated to a temperature of 65°C for durations of $\Delta t = 0$, 30, 60, 120, 180, and 300 seconds. A temperature of 65°C was chosen since it is slightly above the melting temperature of individual staple strands. By heating the 3HB samples for different durations, an increasing fraction of staples are removed, and the structures gradually degrade (Figure 4a). Following the heat shock, the samples were snap-cooled to 4°C to preserve the degraded state, and immediately characterized by gel electrophoresis and nanopore translocation. Figure 4b shows a 1% agarose gel electrophoresis experiment where each lane contains 3HB nanostructures heated for different amounts of time. Structures heated for longer times have higher gel mobility, and contain fast migrating bands, which can be attributed to staples released from the 3HB structure. This confirmed that heat shocks controllably and gradually remove a random subset of staples from 3HB.

Figure 4c shows the corresponding nanopore data, with ΔG_{max} *versus* τ scatter plots for the 3HB nanostructures heat-shocked for $\Delta t = 0$, 30 and 300 seconds, and passing through a 11.4 nm nanopore, in 0.9 M LiCl, under a 400 mV applied voltage. See Supplementary Information Section S11 for the scatter plots of samples degraded for all times tested. The blockades of 3HB

structures before heat shocks ($\Delta t = 0\ s$) show blockages and translocation times consistent with that of Figure 3a: a well-defined single-file population, and a folded population approximately twice as deep displaying a wide τ distribution covering 4 orders of magnitude, indicative of the metastable state. In addition, a few events have maximum blockages centered around $\sim 3 \times \Delta G_1$, corresponding to more complex folded passages, *i.e.* translocation events which at some point during translocation had three segments inside the nanopore at once.

Figure 4c and the corresponding ΔG_{max} histograms shown in Figure 4d reveal that distinct features in the translocation profiles can be observed as the nanostructures are heated. First, the peaks within the ΔG_{max} distributions broaden (making distinct population less easily distinguishable) yet remain consistently centered around the same values. Second, 3HB nanostructures heated for longer periods of time result in more events populating the folded states and consequently less the single-file state. Eventually barely any single-file 3HB events are detected, and mostly complex folding ($> 2 \times \Delta G_1$) is observed, as shown in Figures 4c-d for $\Delta t = 300$ seconds. Lastly, as samples are heat shocked for longer times, translocation events display shorter metastable states: When only heated for 30 seconds, the metastable state is present at the start of many events, yet is significantly shorter than the intact structures, as revealed by the much narrower τ distribution of folded events. For longer heating durations, metastable states become shorter and eventually become undetectable.

This gradual degradation of nanostructures shows that 3HB structures with missing staples have an increased propensity for complex folded translocations. Under controlled experimental conditions, the fraction of translocation events showing complex folding states should give a qualitative insight into the fraction of nanostructures with missing short staple oligomers. Moreover, the reduction and eventual disappearance of metastable states for more degraded samples supports the hypothesis of a heterogeneous rigidity used to explain 3HB folding. By intentionally removing a subset of staple strands, more segments of increased local flexibility should be introduced along the structure. As a result, the average contour distance between the initial docking site and the closest flexible segment should be reduced, in turn reducing the time required for a flexible segment to find the pore through lateral diffusion, and therefore the metastable state duration τ_{META}. Note that although intentionally removing

staples supports the idea that heterogeneous rigidity is responsible for 3HB folding, it does not necessarily imply that missing staples are the cause of weaker spots for fully assembled structures. For example, smaller defects such as nicks (*i.e.* the space between where two neighboring staples end), could be at the root the proposed heterogeneity.[51,52] The nanoscopic distinction between such minute features remain inaccessible to the analysis shown here.

Folded Fraction

Figures 3 and 4 and the corresponding discussions have addressed the potential mechanism and origin of folded 3HB translocations. We now attempt to give insight into the complementary subject of the fraction of folded events (*i.e.* folded fraction) to understand how often 3HB translocates in a single-file or folded fashion. Figure 5a plots the normalized ΔG_{max} histograms for 2 kbp dsDNA and 3HB passing through a 13.3 nm nanopore, in 0.9 M LiCl, under an applied voltage of 200 mV. Recall that these two molecules have similar contour lengths ($L_{3HB} = 820\ nm$, $L_{2kbp} = 680\ nm$). For better visualization, ΔG_{max} values were normalized by the single-file blockage of DNA translocations ΔG_{DNA}. Fitting both histograms to bimodal distributions and comparing the amplitudes of single-file and folded populations, we found that 60% of 3HB translocations, and 36% of 2 kbp translocations were folded. Under the same experimental conditions, 3HB structures therefore translocated in a folded conformation roughly 66% more than 2 kbp. Note that this folded fraction increase was observed for all experiments obtained for this work in which both 3HB and 2 kbp dsDNA were run on the same pore, consistently resulting in 3HB folding 60-80% more than 2 kbp.

As previously stated, folded translocations occur when a molecule enters the nanopore not by its end, but instead by bending a segment along its contour. Understanding the folded fraction of a molecule is therefore equivalent to understanding what factors impact whether a molecule gets captured by an end or not. Here, in order to explain the increased folding fraction observed with 3HB nanostructures, we briefly give insight into the role that polymer rigidity and that non-uniform electric field play in determining a polymer's capture location, *i.e.* where along its contour a polymer first comes into contact with a nanopore.

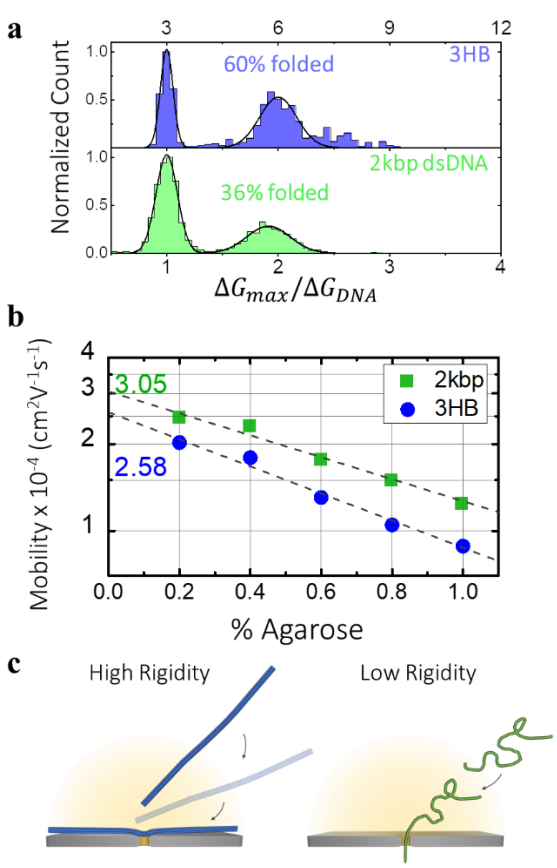

Figure 5. Insights into the fraction of folded 3HB translocations. a) Normalized maximum conductance blockage histograms for 3HB (top) and 2 kbp dsDNA (bottom) in a 13.3 nm pore in 0.9 M LiCl under a 200 mV voltage. The distributions are fit to a bimodal distribution to estimate the fraction of folded events. b) Extrapolation of 3HB and 2 kbp dsDNA free-solution mobility using 0.2 – 1 % Agarose gels. c) Sketch demonstrating the effects of rigidity and on the conformations expected when a slightly misaligned molecule comes into proximity to a pore.

We first consider the role played by the electric field emanating from the nanopore on the conformation of approaching charged polymers. When a voltage is applied across an insulating membrane containing a nanopore, a strong electric field forms within the nanopore and its vicinity. The electric field is strongest inside the pore, and decays as it extends outward radially. The electric field gradient outside of the nanopore can cause both dsDNA and 3HB to approach the pore by an end: For dsDNA, the field gradient stretches out and "unwraps" the polymer as it approaches since the field pulls on the parts of dsDNA that are closer to the pore significantly more than those that are distant.[53–57] For the rigid 3HB molecules, the gradient results in a torque that aligns the 3HB with the field lines.[50,58,59] Similar effects have been seen

for rigid molecules in other nanofluidic devices.[60] For sufficiently strong fields, both molecules are therefore expected to approach the pore by an end in the majority of cases. Generally however, molecules with higher electrophoretic mobility should respond more strongly to the non-uniform electric-field and align with the pore better than molecules of lower mobility, resulting in less folding.

To test whether different electrophoretic mobilities are at the root of 3HB structures consistently folding more than 2 kbp dsDNA, we estimated the free solution mobilities of 3HB and 2 kbp dsDNA molecules by calculating their electrophoretic mobilities μ in agarose gels of different concentrations. For each agarose gel percentages, the distance travelled by the 3HB δx under an applied voltage ΔV was used to estimate the gel-percentage-dependent mobility μ calculated as

$$\mu = \frac{\delta x}{\delta t}\frac{L}{\Delta V}$$

Here, L is the distance between the electrodes applying voltage for a duration of δt. The different mobility measurements were used to extrapolate the 0% gel mobility, *i.e.* the free solution mobility, as shown in Figure 5b. The extrapolation was achieved by fitting the data to an exponential decay function, since electrophoresis for lower gel concentrations is well described by Ogston sieving.[61] The free solution mobility of 3HB structures was extracted to be 2.6×10^{-4} $cm^2V^{-1}s^{-1}$, whereas 2 kbp dsDNA yielded a higher free-solution mobility of 3.1×10^{-4} $cm^2V^{-1}s^{-1}$. These values are in a reasonable agreement with accepted dsDNA mobility values of 3.7×10^{-4} $cm^2V^{-1}s^{-1}$.[62] We therefore estimate the mobility of 3HB structures to be roughly 15% smaller than that of 2 kbp dsDNA.

Since the mobilities of 3HB and 2 kbp dsDNA are of similar values, we instead suggest that, somewhat counter intuitively, the overall increased rigidity of 3HB is responsible for the increased folded translocation fraction. Although both molecules are more likely to approach a nanopore end-first, as discussed, approaching by an end does not guarantee threading by an end. Thermal noise can kick the proximal end of the polymer/nanostructure off track such that it misses the pore. Due to its relative flexibility, dsDNA can still fold and thread through by – or at

least very near – an end even if the initial attempt failed. This is however not possible for the more rigid 3HB molecules. Instead, if the end misses, the molecule's center of mass will continue to approach the pore, eventually resulting in it being pinned against the pore, thereby initiating the metastable state described above. This behavior has been observed in studies of the translocation of rigid filaments through nanopores where even events in which the polymer approached the pore by an end could yield a docked state with the molecules lying against the surface of the membrane on the *cis* side.[50] In accord with this tip deflection scenario, this result was measured to be more likely if the polymer approached the pore at an angle that was oblique relative to the axis of the pore. Through this mechanism, the overall rigidity of 3HB means that even events in which the molecule approaches the pore by an end can result in folded events and thus the more rigid 3HB yields more folded events than 2 kbp dsDNA of similar length.

Conclusion

By thoroughly classifying and analyzing the different types of current signatures for 3-helix bundle (3HB) structures translocating under various conditions, we showed the extent to which DNA nanostructures can be characterized by solid-state nanopores. From the blockage depth and the equivalent charge deficit of single-file translocations, we calculated the volume and the cross-sectional area of 3HB. This substantiated the proper assembly and anticipated dimensions of the nanostructures. Through analysis and the understanding of the 3HB structure folding mechanism, we further revealed that nanopores can give information on the structural rigidity of a DNA nanostructure, which in turn reflects the quality of the assembly. We proposed that 3HB have a heterogeneous rigidity along their contour due to missing a subset of staple strands, allowing for 3HB to fold for nanopore entry. We verified our hypothesis by purposefully removing oligomers from 3HB structures, which resulted in more complex folded translocations (defined as having maximum blockage levels $> 2 \times \Delta G_1$), and facilitated entrance of 3HB into nanopores. Both the metastable state durations and fraction of events showing complex folding sequences are therefore related to the density of missing oligomers along the 3HB structure, or equivalently to the yield of fully assembled structures.

In addition to giving insights on physical characteristics of the 3HB nanostructure, the results shown in this work outline the role of rigidity in the nanopore capture and translocation process. Our results suggest that docked polymers , when incapable of bending and entering a nanopore, can diffuse laterally along their contour while remaining atop the pore due to the strong electrophoretic pull. Under these circumstances, the contour of the rigid polymer is scanned by the nanopore until a segment and conformation are found that favors translocation, either by an end or by folding. Therefore, in addition to conformational entropy,[46] rigidity should accentuate the energetic contributions required for initiating the translocation process, and as a result should alter the statistics of where along its contour a polymer folds when entering a nanopore.

We note that similar docking behavior has been observed recently by Shi *et al*,[48] who showed that 6-helix bundle structures could dock on top of solid-state nanopores, and undergo rotary motion due to the competing effects of electrophoresis and electroosmosis under the presence of a potential gradient, or of diffusiophoresis and diffusioosmosis in the presence of a salt concentration gradient. In addition to lateral diffusion, rotational motion could indeed occur during the outlined metastable state, however evidence of such behavior could not be detected when looking only at ionic current signatures due to the cylindrical symmetry of the nanopore.

Finally, we hope that our results show how the plurality of signals obtained by nanopore translocations contain rich information about the dimensions of an analyte and its rigidity and will further motivate their use for characterizing more complex DNA origami nanostructures.

Methods

Scaffold Preparation

The linearized M13 single-stranded DNA scaffolds were prepared from M13mp18 circular single-stranded DNA (New England Biolabs, N4040S). To attach the primer, primer strand was added in a mixture with 10 μg M13mp18 circular single-stranded DNA at a ratio of 10:1 in 1x NEB 3.1 buffer, the mixture was heated to 95 ^{o}C, and slowly cooled down to room temperature in a MiniAmp Plus Thermal Cycler (ThermoFisher Scientific, #A37835). A mixture of prepared circular scaffold (with primer attached), and 10 units of HincII restriction enzyme (New England Biolabs,

R0103S) in a total reaction volume of 50 μL in 1x NEB 3.1 buffer were incubated at 37 ^{o}C for 3 hours, then heat-inactivated at 65 ^{o}C for 20 minutes in the thermal cycler.

The linearized products were characterized by denaturing agarose gel electrophoresis at 1% in 1x TAE buffer (40 mM Tris, 20 mM acetic acid, and 2 mM EDTA, pH 10.5). Upon completion, the agarose gel was submerged in 1xTAE buffer (40 mM Tris, 20 mM acetic acid, and 2 mM EDTA) at pH 8 and incubated on incubator at 60 RPM for an hour to bring gel pH back to 8. The gel was then submerged in 2x gel volume de-ionized water with 1x GelRed (Biotium, #41003) for 45 minutes on incubator then store at 4 ^{o}C overnight to post stain. As shown in Supplementary Figure S1, linear single-stranded M13 migrate faster than circular single-stranded M13 molecules, the disappearance of circular band is an indication of complete cut. The sequence of the linearized M13 scaffold is provided in Supplementary Information section S1.

Nanostructure Assembly

For the assembly of the 3HB molecules, the scaffold (linearized M13mp18 from New England Biolabs, N4040S) was mixed with 191 staple strands at a molar ratio of 1:10 in assembly buffer (at final 40 mM Tris, 20 mM acetic acid, 2 mM EDTA, and 16 mM $MgCl_2$, pH 8). The product is heated to 95 ^{o}C for 5 minutes, cooled to 90 ^{o}C, ramped from 90 ^{o}C to 60 ^{o}C at a rate of 0.4 ^{o}C per minute, then from 60 ^{o}C to 26 ^{o}C at a rate of 0.03 ^{o}C, and snap cooled to 4 ^{o}C using minicamp Plus Thermal Cycler (ThermoFisher Scientific, #A37835). After the assembly, the nanostructures were spun down using 100 kDa Amicon Ultra-0.5 Centrifugal Filter Unit (Millipore Sigma, UFC500396), three washes with the assembly buffer were performed to completely remove excess staple strands present in the solution. The assembled products were visualized on 1% agarose gel in 1x TAE buffer (40 mM Tris, 20 mM acetic acid, and 2 mM EDTA, pH 8), as shown in Supplementary Section 1. Generuler 1 kb plus DNA Ladder (ThermoFisher Scientific, SM1331) was used as a reference guide for nanostructure migration. GelRed (Biotium, #41003) was used for visualization of the DNA bands.

Nanopore Fabrication

Nanopores were fabricated in 12 nm thick free-standing SiN_x membranes (Norcada, NBPX5004Z) using the controlled breakdown (CBD) method.[27,28,31,32] CBD was performed in 1 M

KCl buffered with 10 mM HEPES at pH 8 and pores were grown to 9–15 nm in 3.6 M LiCl buffered with 10 mM HEPES at pH 8 using moderate voltage conditioning, using Spark-E2 instruments and flow cells similar to products from Northern Nanopore Instruments (NNi) as described in Waugh *et al*.[41] The uncertainties of pore diameters are calculated to be 0.5 nm, or smaller, for every pore used in this work, using NNi online calculator (https://www.solidstatenanopore.com/nanopore-calculator). Prior to fabrication, the chips were cleaned using air plasma for 70 s and painted with a layer of PDMS to reduce high-frequency noise.

Nanopore Sensing

The DNA nanostructures in 1x assembly buffer were added to a LiCl solution of 0.45 M to 3.6 M for nanopore sensing, typically $5\ \mu L$ of the nanostructure solution was added to $35\ \mu L$ LiCl buffered with 10 mM HEPES at pH 8. Linear 2 kbp (ThermoFisher Scientific, SM1701) and 7 kbp (ThermoFisher Scientific, SM1741) NoLimits DNA fragments were always run prior to nanostructures or in a mixture to normalize pore geometry variations during post-processing. Samples were introduced to the *cis* side of the chip and a negative voltage was applied to the *cis* side with the *trans* side grounded. The ionic current recordings were performed in MATLAB 2013a (32-bit) using the VC100 current amplifier (Chimera Instruments) with sampling frequency of 4.17 MHz and a bandwidth of 1 MHz and were subsequently software low-pass Bessel filtered as needed.

Data Analysis

Translocation events in the recorded current traces were located and fitted using a custom implementation of the CUSUM+ algorithm.[33] A digital low-pass filter of 200 kHz was applied for the analysis unless otherwise specified. The fitted translocation events were plotted and further analyzed using Nanolyzer (v0.1.41) from Northern Nanopore Instruments and Origin 2016 from OriginLab.

Author Contributions

Conceived the project and designed the experiments: V.T.-C, L.H, M.C., and K.B.; Designed DNA origami assembly protocol and prepared structures: L.H.; Performed nanopore experiments: L.H.; Analyzed nanopore data: M.C., and L.H.; Provided insights and interpretation for the understanding of data: M.C, P.K., V.T.-C., J.A. and H.dH. The manuscript was written through contributions of all authors. All authors have given approval of the final version of the manuscript.

Conflicts of interest

K.B. and V.T.-C. are, respectively, the CEO and CSO of Northern Nanopore Instruments Inc., a for-profit company that provides solid-state nanopore tools and software. L.H, M.C., P.K., J.A. and H.dH declare no conflicts of interest.

Acknowledgements

The authors would like to acknowledge the support of the Natural Sciences and Engineering Research Council of Canada (NSERC), through funding from grant #CRDPJ 530554-18. M.C. thanks the Ontario Graduate Scholarship (OGS) Program. The authors would like to thank Gary Slater for fruitful discussions.

References

1. Seeman, N. C. Nucleic acid junctions and lattices. *J. Theor. Biol.* **99**, 237–247 (1982).
2. Dey, S. *et al.* DNA origami. *Nat. Rev. Methods Prim.* **1**, 13 (2021).
3. Seeman, N. C. & Sleiman, H. F. DNA nanotechnology. *Nat. Rev. Mater.* **3**, (2017).
4. Rothemund, P. W. K. Folding DNA to create nanoscale shapes and patterns. (2006) doi:10.1038/nature04586.
5. Ke, Y., Ong, L. L., Shih, W. M. & Yin, P. Three-dimensional structures self-assembled from DNA bricks. *Science (80-.).* **338**, 1177–1183 (2012).
6. Wintersinger, C. M. *et al.* Multi-micron crisscross structures grown from DNA-origami slats. *Nat. Nanotechnol. 2022* 1–9 (2022) doi:10.1038/s41565-022-01283-1.
7. Douglas, S. M., Chou, J. J. & Shih, W. M. DNA-nanotube-induced alignment of membrane proteins for NMR structure determination. *Proc. Natl. Acad. Sci. U. S. A.* **104**, 6644–6648 (2007).

8. Liedl, T., Högberg, B., Tytell, J., Ingber, D. E. & Shih, W. M. Self-assembly of three-dimensional prestressed tensegrity structures from DNA. *Nat. Nanotechnol. 2010 57* **5**, 520–524 (2010).

9. Gu, H., Yang, W. & Seeman, N. C. DNA scissors device used to measure mutS binding to dna mis-pairs. *J. Am. Chem. Soc.* **132**, 4352–4357 (2010).

10. Chhabra, R., Sharma, J., Liu, Y. & Yan, H. Addressable molecular tweezers for DNA-templated coupling reactions. *Nano Lett.* **6**, 978–983 (2006).

11. Andersen, E. S. *et al.* Self-assembly of a nanoscale DNA box with a controllable lid. *Nat. 2009 4597243* **459**, 73–76 (2009).

12. Li, S. *et al.* A DNA nanorobot functions as a cancer therapeutic in response to a molecular trigger in vivo. *Nat. Biotechnol. 2018 363* **36**, 258–264 (2018).

13. Hansen, C. H., Yang, D., Koussa, M. A. & Wong, W. P. Nanoswitch-linked immunosorbent assay (NLISA) for fast, sensitive, and specific protein detection. *Proc. Natl. Acad. Sci. U. S. A.* **114**, 10367–10372 (2017).

14. Shrestha, P. *et al.* Single-molecule mechanical fingerprinting with DNA nanoswitch calipers. *Nat. Nanotechnol.* **16**, 1362–1370 (2021).

15. Mathur, D. & Medintz, I. L. Analyzing DNA Nanotechnology: A Call to Arms for the Analytical Chemistry Community. *Anal. Chem.* **89**, 2646–2663 (2017).

16. Woeste, S. & Demchick, P. New version of the negative stain. *Appl. Environ. Microbiol.* **57**, 1858–1859 (1991).

17. De Carlo, S. & Harris, J. R. Negative staining and cryo-negative staining of macromolecules and viruses for TEM. *Micron* **42**, 117–131 (2011).

18. Stirling, J. W., Curry, A. & Eyden, B. Diagnostic electron microscopy : a practical guide to tissue preparation and interpretation. (2013).

19. Harris, J. R. & De Carlo, S. Negative Staining and Cryo-negative Staining: Applications in Biology and Medicine. *Methods Mol. Biol.* **1117**, 215–258 (2014).

20. Douglas, S. M. *et al.* Self-assembly of DNA into nanoscale three-dimensional shapes. *Nature* **459**, 414–418 (2009).

21. Castro, C. E. *et al.* A primer to scaffolded DNA origami. *Nat. Methods* **8**, 221–229 (2011).

22. Dietz, H., Douglas, S. M. & Shih, W. M. Folding DNA into twisted and curved nanoscale shapes. *Science (80-.).* **325**, 725–730 (2009).

23. Alibakhshi, M. A. *et al.* Picomolar Fingerprinting of Nucleic Acid Nanoparticles Using Solid-State Nanopores. *ACS Nano* **11**, 9701–9710 (2017).

24. He, L., Karau, P. & Tabard-Cossa, V. Fast capture and multiplexed detection of short multi-arm DNA stars in solid-state nanopores. *Nanoscale* **11**, 16342–16350 (2019).

25. Beamish, E., Tabard-Cossa, V. & Godin, M. Identifying Structure in Short DNA Scaffolds Using Solid-State Nanopores. *ACS Sensors* **2**, 1814–1820 (2017).

26. Bell, N. A. W. & Keyser, U. F. Digitally encoded DNA nanostructures for multiplexed, single-molecule protein sensing with nanopores. *Nat. Nanotechnol.* **11**, 645–651 (2016).

27. Raveendran, M., Lee, A. J., Sharma, R., Wälti, C. & Actis, P. Rational design of DNA nanostructures for single molecule biosensing. doi:10.1038/s41467-020-18132-1.

28. He, L. *et al.* Digital immunoassay for biomarker concentration quantification using solid-state nanopores. *Nat. Commun. 2021 121* **12**, 1–11 (2021).

29. Beamish, E., Tabard-Cossa, V. & Godin, M. Digital counting of nucleic acid targets using solid-state nanopores. *Nanoscale* **12**, 17833–17840 (2020).

30. Beamish, E., Tabard-Cossa, V. & Godin, M. Programmable DNA Nanoswitch Sensing with Solid-State Nanopores. *ACS Sensors* **4**, 2458–2464 (2019).

31. He, L. *et al.* Digital Immunoassay Protocol for Solid-State Nanopore Sensing. *Protoc. Exch.* (2021).

32. Hernández-Ainsa, S. *et al.* DNA origami nanopores for controlling DNA translocation. *ACS Nano* **7**, 6024–6030 (2013).

33. He, L. DNA Nanostructures for Nanopore-based Digital Assays. (2022).

34. Zhu, J. *et al.* Image Encoding Using Multi-Level DNA Barcodes with Nanopore Readout. *Small* **17**, 2100711 (2021).

35. Chen, K. *et al.* Digital Data Storage Using DNA Nanostructures and Solid-State Nanopores. *Nano Lett.* **19**, 1210–1215 (2019).

36. Doricchi, A. *et al.* Emerging Approaches to DNA Data Storage: Challenges and Prospects. *ACS Nano* **16**, 17552–17571 (2022).

37. Kundukad, B., Yan, J. & Doyle, P. S. Effect of YOYO-1 on the mechanical properties of DNA. *Soft Matter* **10**, 9721–9728 (2014).

38. Japaridze, A., Benke, A., Renevey, S., Benadiba, C. & Dietler, G. Influence of DNA binding dyes on bare DNA structure studied with atomic force microscopy. *Macromolecules* **48**, 1860–1865 (2015).

39. Douglas, S. M. *et al.* Rapid prototyping of 3D DNA-origami shapes with caDNAno. *Nucleic Acids Res.* **37**, 5001–5006 (2009).

40. Kwok, H., Briggs, K. & Tabard-Cossa, V. Nanopore fabrication by controlled dielectric breakdown. *PLoS One* **9**, e92880 (2014).

41. Waugh, M. *et al.* Solid-state nanopore fabrication by automated controlled breakdown. *Nat. Protoc.* **15**, 122–143 (2020).

42. Li, J., Gershow, M., Stein, D., Brandin, E. & Golovchenko, J. A. DNA molecules and configurations in a solid-state nanopore microscope. *Nat. Mater.* **2**, 611–615 (2003).

43. Schmid, S., Stömmer, P., Dietz, H. & Dekker, C. Nanopore electro-osmotic trap for the label-free study of single proteins and their conformations. *Nat. Nanotechnol.* **16**, 1244–1250 (2021).

44. Smeets, R. M. M. *et al.* Salt dependence of ion transport and DNA translocation through solid-state nanopores. *Nano Lett.* **6**, 89–95 (2006).

45. Kowalczyk, S. W., Wells, D. B., Aksimentiev, A. & Dekker, C. Slowing down DNA translocation through a nanopore in lithium chloride. *Nano Lett.* **12**, 1038–1044 (2012).

46. Mihovilovic, M., Hagerty, N. & Stein, D. Statistics of DNA capture by a solid-state nanopore. *Phys. Rev. Lett.* **110**, 1–5 (2013).

47. Kowalczyk, S. W. & Dekker, C. Measurement of the docking time of a DNA molecule onto a solid-state nanopore. *Nano Lett.* **12**, 4159–4163 (2012).

48. Shi, X. *et al.* Sustained unidirectional rotation of a self-organized DNA rotor on a nanopore. *Nat. Phys.* **18**, 1105–1111 (2022).

49. Hernández-Ainsa, S., Misiunas, K., Thacker, V. V., Hemmig, E. A. & Keyser, U. F. Voltage-dependent properties of DNA origami nanopores. *Nano Lett.* **14**, 1270–1274 (2014).

50. Mcmullen, A., De Haan, H. W., Tang, J. X. & Stein, D. Stiff filamentous virus translocations through solid-state nanopores. *Nat. Commun.* (2014) doi:10.1038/ncomms5171.

51. Lee, C., Kim, K. S., Kim, Y. J., Lee, J. Y. & Kim, D. N. Tailoring the Mechanical Stiffness of DNA Nanostructures Using Engineered Defects. *ACS Nano* **13**, 8329–8336 (2019).

52. Penth, M., Schellnhuber, K., Bennewitz, R. & Blass, J. Nanomechanics of self-assembled DNA building blocks. *Nanoscale* **13**, 9371–9380 (2021).

53. Farahpour, F., Maleknejad, A., Varnik, F. & Ejtehadi, M. R. Chain deformation in translocation phenomena. *Soft Matter* **9**, 2750–2759 (2013).

54. Vollmer, S. C. & De Haan, H. W. Translocation is a nonequilibrium process at all stages: Simulating the capture and translocation of a polymer by a nanopore. *J. Chem. Phys.* **145**, (2016).

55. Charron, M., Philipp, L., He, L. & Tabard-Cossa, V. Elucidating the dynamics of polymer transport through nanopores using asymmetric salt concentrations. *Nano Res.* (2022) doi:10.1007/s12274-022-4886-3.

56. Seth, S. & Bhattacharya, A. How capture affects polymer translocation in a solitary nanopore. *J. Chem. Phys.* **156**, 244902 (2022).

57. Afrasiabian, N. & Denniston, C. The journey of a single polymer chain to a nanopore. *Soft Matter* **16**, 9101–9112 (2020).

58. Qiao, L. & Slater, G. W. Capture of rod-like molecules by a nanopore: Defining an ‘orientational capture radius’. *J. Chem. Phys.* **152**, (2020).

59. Qiao, L. & Slater, G. W. Capture and translocation of a rod-like molecule by a nanopore: orientation, charge distribution and hydrodynamics. *Phys. Chem. Chem. Phys.* **24**, 6444–6452 (2022).

60. Dorfman, K. D. DNA electrophoresis in microfabricated devices. *Rev. Mod. Phys.* **82**, 2903–2947 (2010).

61. Functionalizable, A. C. *et al.* Polyacrylamide Gel Electrophoresis. **283**, 1148–1150 (2016).

62. Stellwagen, N. C., Gelfi, C. & Righetti, P. G. The free solution mobility of DNA. *Biopolymers* **42**, 687–703 (1997).